# The First Bump-Bonded Pixel Detectors on CVD Diamond


**The RD42 Collaboration**

W. Adam[1], C. Bauer[2], E. Berdermann[3], P. Bergonzo[4], F. Bogani[5], E. Borchi[6], A. Brambilla[4], M. Bruzzi[6], C. Colledani[7], J. Conway[8], W. Dabrowski[9], P. Delpierre[10], A. Deneuville[11], W. Dulinski[7], B. van Eijk[12], A. Fallou[10], F. Fizzotti[13], F. Foulon[4], M. Friedl[1], K.K. Gan[14], E. Gheeraert[11], E. Grigoriev[9], G. Hallewell[10], R. Hall-Wilton[15], S. Han[14], F. Hartjes[12], J. Hrubec[1], D. Husson[7], H. Kagan[14], D. Kania[14], J. Kaplon[9], C. Karl[16], R. Kass[14], M. Krammer[1], A. Logiudice[13], R. Lu[13], P.F. Manfredi[17], C. Manfredotti[13], R.D. Marshall[4], D. Meier[9], M. Mishina[18], A. Oh[16], V.G. Palmieri[19], L.S. Pan[14]A. Peitz[8], M. Pernicka[1], S. Pirollo[6], P. Polesello[13], K. Pretzl[19], V. Re[17], J.L. Riester[7], S. Roe[9], D. Roff[15], A. Rudge[9], S. Schnetzer[8], S. Sciortino[6], V. Speziali[17], H. Stelzer[3], J. Steuerer[16], R. Stone[8], R.J. Tapper[15], R. Tesarek[8], M. Trawick[14], W. Trischuk[20]†, R. Turchetta[7], E. Vittone[13], A. Wagner[16], A.M. Walsh[8], R. Wedenig[9], P. Weilhammer[9], W. Zeuner[16], H. Ziock[21], M. Zoeller[14]

**in collaboration with**

E. Charles[22], A. Ciocio[23], K. Dao[22], K. Einsweiler[23], D. Fasching[22], M. Gilchriese[23], A. Joshi[23], S. Kleinfelder[23], O. Milgrome[23], N. Palaio[23], J. Richardson[23], P. Sinervo[20], G. Zizka[23]

[1] *Institut für Hochenergiephysik der Österr. Akademie d. Wissenschaften, A-1050 Vienna, Austria*
[2] *MPI für Kernphysik, D-69029 Heidelberg, Germany*
[3] *GSI, Darmstadt, Germany*
[4] *LETI (CEA-Technologies Avancees) DEIN/SPE - CEA Saclay, 91191 Gif-Sur-Yvette, France*
[5] *LENS, Florence, Italy*
[6] *University of Florence, Florence, Italy*
[7] *LEPSI, CRN, Strasbourg 67037, France*
[8] *Rutgers University, Piscataway, NJ 08855, U.S.A.*
[9] *CERN, CH-1211, Geneva 23, Switzerland*
[10] *CPPM, Marseille 13288, France*
[11] *LEPES, Grenoble, France*
[12] *NIKHEF, Amsterdam, Netherlands*
[13] *Univerity of Torino, Italy*
[14] *The Ohio State University, Columbus, OH 43210, U.S.A.*
[15] *Bristol University, Bristol BS8 1TL, U.K.*
[16] *DESY, Hamburg, Germany*
[17] *Universita di Pavia, Dipartimento di Eletronica, 27100 Pavia, Italy*
[18] *FNAL, Batavia, U.S.A.*
[19] *Lab. für Hochenergiephysik, 3012 Bern, Switzerland*
[20] *University of Toronto, Toronto, ON M5S 1A7, Canada*
[21] *Los Alamos National Laboratory, Research Division, Los Alamos, NM 87545, U.S.A.*
[22] *The University of Wisconsin, Madison, WI 53706, U.S.A.*
[23] *Lawrence Berkeley National Laboratory, Berkeley, CA 94720, U.S.A.*

† Corresponding author, tel. 1-(416)-978-8095, fax 1-(416)-978-8221

**Abstract**

Diamond is a nearly ideal material for detecting ionising radiation. Its outstanding radiation hardness, fast charge collection and low leakage current allow it to be used in high radiation environments. These characteristics make diamond sensors particularly appealing for use in the next generation of pixel detectors. Over the last year, the RD42 collaboration has worked with several groups that have developed pixel readout electronics in order to optimise diamond sensors for bump-bonding. This effort resulted in an operational diamond pixel sensor that was tested in a pion beam. We demonstrate that greater than 98% of the channels were successfully bump-bonded and functioning. The device shows good overall hit efficiency as well as clear spatial hit correlation to tracks measured in a silicon reference telescope. A position resolution of 14.8$\mu$m was observed, consistent with expectations given the detector pitch.

# 1 Introduction

Pixel detectors facilitate pattern recognition and vertexing in locations where the track occupancy in strip detectors would be too high or bulk radiation damage too great. At present the ATLAS [1] and CMS [2] experiments at the Large Hadron Collider (LHC) and the BTeV [3] experiment at the Fermilab Tevatron plan to install pixel devices as the innermost layers of their tracking detector. Substituting chemical vapour deposited (CVD) diamond sensors for silicon would preserve the advantages of solid-state tracking such as precision and stability and extend the life of these sensors that would otherwise be limited by radiation damage [4].

In the presently envisaged ATLAS pixel detectors [5] each pixel cell will be read out by an individual charge sensitive preamplifier followed by a 25 ns peaking time shaper. The shaped signals will then be evaluated by sparsification logic, digitised and transmitted out of the interaction region. The pixel detector readout chip must geometrically match the pixel pattern on the detector substrate so that a single active cell on the detector substrate can be connected to its readout cell via a bump-bond. On the 50 $\mu$m scale required for these detectors, bump-bonding is a non-trivial process.

The first diamond pixel detector was tested in August 1996 in a particle beam at CERN [4, 6]. This test investigated the feasibility of pixel geometries on diamond substrates and studied charge collection performance. At that time, bump-bonding was not yet possible on small parts. As a result, this detector was readout by VA2 strip electronics [7] via a wire-bonded fanout structure metallised on a glass substrate. The devices had a pitch of $150 \times 150\ \mu\text{m}^2$. A typical device had a mean signal-to-noise ratio of 27:1 and a position resolution of better than 50 $\mu$m consistent with the digital resolution for 150 $\mu$m pitch. The residuals between tracks in a silicon reference telescope and the position reported by the diamond pixel detector are shown in Fig. 1. We observed good spatial correlation between hits recorded by the diamond pixel detector and external reference tracks. Based on the success of this test, we produced pixel sensors to the specifications of ATLAS and CMS. The contact geometry on the diamond surface was fabricated to match the requirements of the existing prototype readout chips for ATLAS and CMS.

In this paper, we present the first results of a diamond pixel detector bump-bonded to prototype LHC readout electronics.

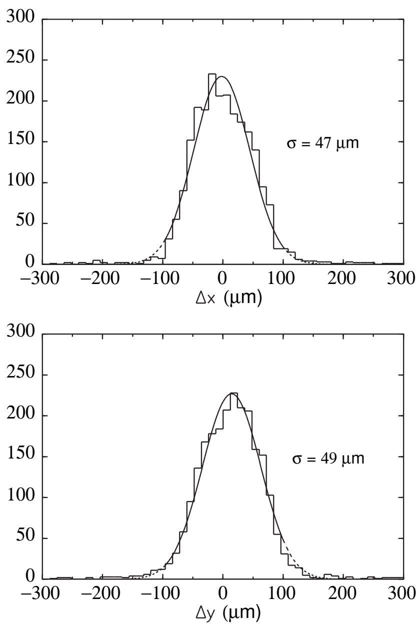


Figure 1: Position resolution ($\Delta x$, $\Delta y$) of the first diamond pixel detector read out with a glass routing structure to strip electronics along the sides of the sensor.

## 2 Sensor Preparation

Table 1 gives an overview of the diamond sensors prepared. The metallisation contact and bump-bonding metal are listed for reference.

| | pixel pitch [$\mu$m$^2$] | diamond substrate size [$\mu$m$^2$] | metallisation [elements] | passivation | bump-bonding metal |
|---|---|---|---|---|---|
| CMS/1 | 125 × 125 | 3725 × 4725 | Cr/Au | yes | In |
| ATLAS/1 | 50 × 433.4 | 3800 × 5800 | Cr/Ni/Au | yes | Sn/Pb |
| ATLAS/2 | 50 × 433.4 | 3800 × 5800 | Ti/W | no | In |
| ATLAS/3 | 50 × 536 | 4000 × 8000 | Ti/W | no | In |

Table 1: Overview of diamond pixel sensors prepared for work with the CMS and ATLAS pixel electronics. The dimensions of the sensors, their metallisation and passivation layers are listed.

The first bump-bonding tests were performed in collaboration with groups from the CMS experiment. Chromium/gold was chosen for the pixel metallisation since chromium has been used in diamond strip trackers [6] as it forms a good ohmic contact with the diamond surface while gold provides a bondable inert over-layer. Bump-bonding tests were performed at the Paul Scherer Institute near Zurich. Figure 2 shows the first diamond pixel sensor prepared for the CMS/1 readout electronics. A visual inspection of the bumps deposited on this device showed that a significant fraction of the bonds were viable. Recent developments have made this process more reliable so that a working prototype should be

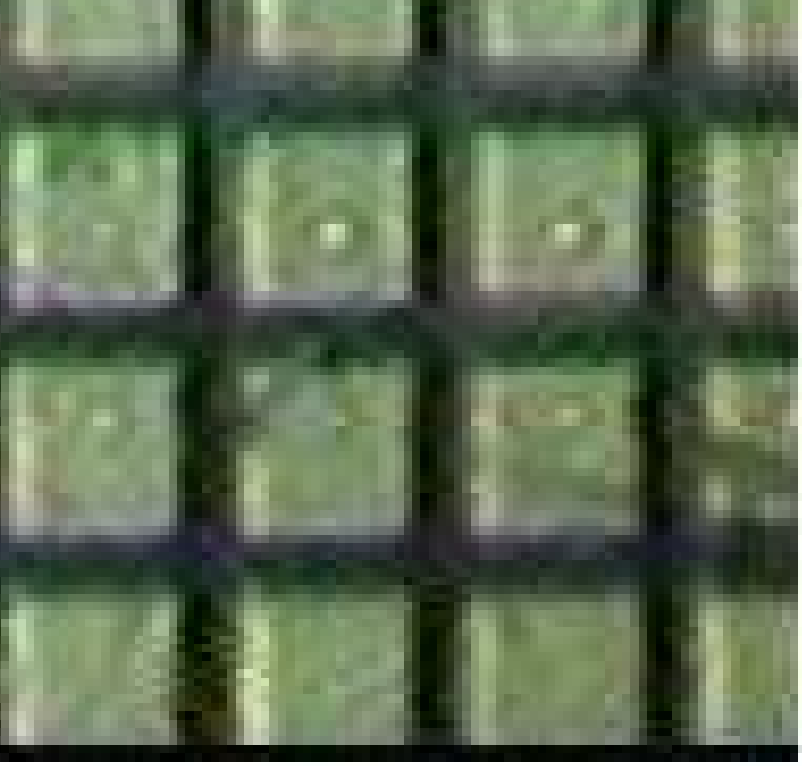

Figure 2: Top view of a CMS diamond pixel sensor showing the overall pixel pattern. The pixel metallisation was Cr/Au. The pixels were covered with a passivation layer. The passivation layer had a hole offset from the pixel center into which the indium bump was deposited.

produced in the future.

Additional devices were bump-bonded in industry at Boeing [8]. Silicon sensors previously bonded by Boeing using their process have exhibited failure probabilities of less than $10^{-4}$ per bond. Figure 3 shows the first diamond pixel sensor with a pixel metallisation pattern for the ATLAS/3 readout electronics. This pixel sensor was produced with titanium/tungsten (Ti/W) metallisation and successfully bonded to an ATLAS/3 pixel readout chip. The choice of Ti/W for the detector metallisation was also natural for bump-bonding on diamond sensors since Ti creates a good ohmic contact with the diamond surface, facilitating the extraction of the signal, while W is an inert over-metal that is commonly used in integrated circuit processing. Tungsten also resists oxidation, a feature necessary as the diamond sensors were prepared in a different location than the final bump-bonding.

In the Boeing bump-bonding process, the W is lightly etched and a photo-resist layer is deposited on the surface. Photolithography is used to open regions in the photoresist for indium deposition. Indium is evaporated onto the entire surface and the photo-resist is lifted off leaving $\sim 20\ \mu$m diameter indium bumps. A visual inspection of the indium bumps on the diamond device showed a yield of 100%. A similar process was used to deposit indium on the readout electronics. The two pieces were flipped and aligned to bring pairs of indium bumps into contact. They were then cold fused with pressure. The bonds that were formed are typically $\sim 12\ \mu$m high.

Figure 3: A view of the ATLAS/3 diamond pixel sensor showing the overall pixel pattern including a section of the guard ring and the staggered columns. The pixel metallisation was Ti/W. The pixels were not covered with a passivation layer.

## 3 Diamond Sample Properties

The chemical vapour deposition (CVD) diamond used in these tests was provided by the DeBeers Industrial Diamond Division [9]. This material is polycrystalline in nature with expanding crystallites that begin with small grains ($\sim 1\mu$m) on the substrate side and terminate with large grains ($\sim 100\mu$m) on the growth side. The diamond sample used was grown to a thickness of 1060 $\mu$m. To prepare the material for pixel patterning the growth side was planarised and material was removed from the substrate side. The electrical properties in CVD diamond increase roughly linearly through the bulk of the material [10, 11]. Thus, removing material from the substrate side increases the average quality of the diamond and makes it more uniform. For the diamond used in the ATLAS/3 pixel detector, 100 $\mu$m was removed from the growth side and 350 $\mu$m was removed from the substrate side. This procedure left the diamond with a thickness of 610 $\mu$m. The surface was flat with features smaller than 1 $\mu$m as determined by inspection with an optical microscope.

Another important property of CVD diamond is that the signal generated by the passage of a charged particle can be enhanced through prior exposure of the sample to ionising radiation. This property, referred to as "pumping" [11, 12], is understood to be due to the filling of charge trapping centres in the diamond material during the prior exposure. Subsequent charges moving through the detector are able to travel further inducing larger signals on electrodes on the diamond surface. Once a sample is pumped-up, the charge trapping centres remain filled until the sample is exposed to certrain frequencies of light. Thus, the pumped-up state is stable if the detector is operated in a light-tight box. Pumped-up CVD diamond samples typically yield signals 1.6 times larger than samples in the un-pumped state [12].

The diamond used in the ATLAS/3 pixel detector went through a selection procedure that involved first characterising the sample with solid electrodes on each side, then patterning it for use as a strip detector and testing it in a pion beam and finally re-patterning it as a pixel detector. The quality of a diamond is given by the charge collection distance [10, 12], $\bar{d}$, the average distance an electron and hole move apart under the influence of an external electric field. In diamond, $\bar{d}$ is related to the charge observed, $Q$, by

$$\bar{d} = \frac{Q}{36e/\mu\mathrm{m}}. \tag{1}$$

In Fig. 4, we plot the charge collection distance versus electric field for the diamond sample used to make the ATLAS/3 pixel detector, measured using electrons from a $^{90}$Sr source. A description of the apparatus used to make these measurements can be found in [12]. The charge collection distance increases with increasing electric field. At approximately 1.0 V/$\mu$m, the charge collection begins to saturate as the carrier velocity saturates. The charge collection distance from this sample was measured to be 160 $\mu$m at an electric field of 1 V/$\mu$m corresponding to a mean charge signal of 5800 $e$ for a minimum ionising particle.

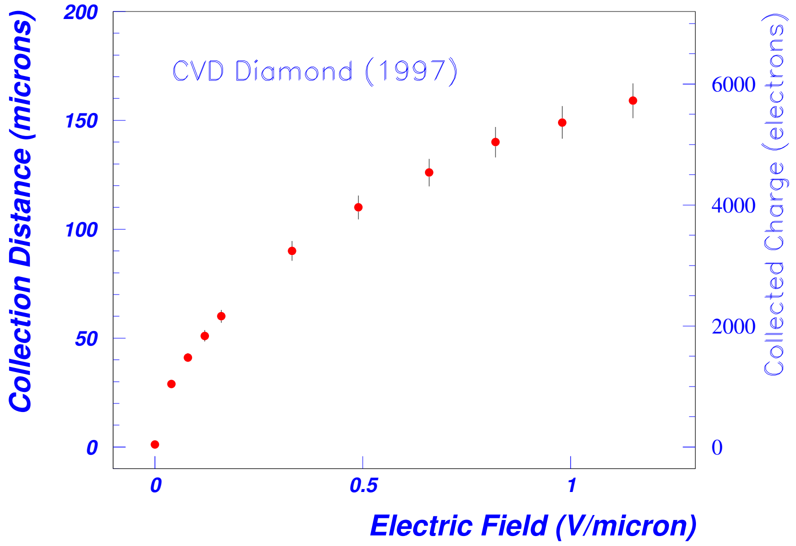


Figure 4: The collection distance versus electric field for the diamond used in the ATLAS/3 pixel detector. For this measurement solid electrodes were used on each side and a $^{90}$Sr source provided approximately minimum ionising particles traversing the diamond. The diamond was in the pumped-up state when this measurement was made (see text).

## 4 The ATLAS/3 Pixel Readout Electronics

The ATLAS/3 readout chip that was bump-bonded to the diamond sensor consisted of twelve columns of sixty-four pixels each. The pixels had a pitch of 50 $\mu$m by 536 $\mu$m and alternate rows of pixels were staggered (see Fig. 3). The information from each column of pixels was read out using end-of-column logic that occupied about 2 mm along one edge of the chip. Data and control signals were connected via wire-bonds along the lower edge of the readout chip, while analog biasing was supplied via wire bonds along the upper edge of the chip. This required that the pixel pattern extend to within 0.5 mm of two edges of the diamond sensor so that wire-bond connections could be made after the sensor and readout chip had been bump-bonded.

The readout chip was developed at LBL and fabricated using the Hewlett-Packard 0.8 $\mu$m triple-metal CMOS process [13]. The input stage was a very high gain, charge sensitive amplifier with a 2 fF feedback capacitor with a peaking time of about 40 ns. The amplifier provided a linear time-over-threshold (TOT) measurement of the signal amplitude for pulses ranging from less than 1 fC to more than 10 fC. The pre-amplifier was DC-coupled to a discriminator that was optimised to provide a stable threshold and reasonably small threshold dispersion from pixel to pixel. For pixels that exceeded the threshold, the TOT information was stored on an internal capacitor. The charge and address information for hits were associated with a particular beam crossing clock cycle by storing a 3-bit counter in the pixel and an 8-bit crossing counter in the end of column logic. The hit information remained in the pixel until the chip received a readout trigger signal after a latency of 3.2 $\mu$s. After the trigger arrived, a two dimensional sparse scan of all the pixel channels was initiated to transfer the address (digital row and column number) and charge (analog TOT) information off the chip for those pixels that were above threshold. The analog TOT information was buffered on the chip and digitised by an 8-bit flash ADC on a nearby readout card, prior to being recorded by the data acquisition system.

## 5 Results from Lab Tests

The first test of the ATLAS/3 pixel detector was performed using a $^{107}$Ru source at CERN in late 1997. The relatively low electron end point energy of this source (3.54 MeV) meant that it was not possible to include a silicon reference plane between the pixel prototype and the trigger. Thus, no external spatial information was available in this initial test. The source was mounted 5 cm from the surface of the pixel detector. A $7 \times 7$ mm$^2$ scintillator trigger counter was mounted 3 cm behind the pixel detector. In order to quantify the trigger acceptance and efficiency, a silicon pixel detector with the same readout chip was tested first. We took about 15,000 triggers in the silicon test run. We observed 5,100 hits in the silicon pixel detector which corresponds to the 35 % geometric acceptance expected from the ratio of the active area of the pixel detector (17.3 mm$^2$) relative to the area of the trigger counter (49 mm$^2$).

We then focused on the diamond pixel detector. During this source test the threshold on the readout chip bonded to the diamond sensor could not be set below 4,500 $e^-$. Further, to protect the readout electronics which was not implemented in a radiation hard technology, we were reluctant to either operate the diamond pixel device at full voltage or

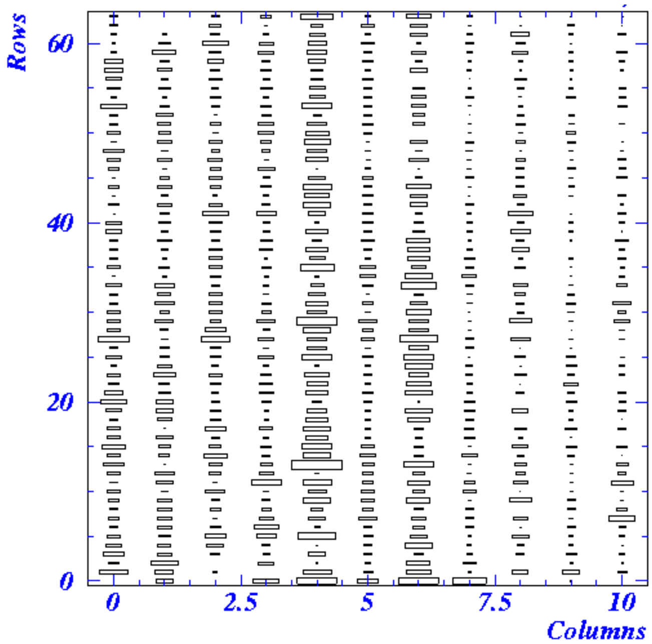


Figure 5: Distribution of hits per pixel seen in the 1998 testbeam. The area of the boxes is proportional to the number of hits seen in each pixel.

to expose the device to any significant radiation. Thus, during this test the threshold was approximately a factor of two higher than optimal and the signal from the un-pumped diamond was a factor of 1.6 lower than had been observed in previous tests of this sensor. Despite these limitations, a run of 39,000 triggers yielded hits in 75 % of the pixels with a hit density consistent with the source beam profile. Poisson fluctuations on the small number of hits per pixel observed could explain the hits missing from a further 15 % of the pixels. This result was sufficiently encouraging to invest further effort to install the pixel detector in the testbeam.

## 6 Testbeam Results

The ATLAS/3 pixel diamond detector was tested in a 50 GeV pion beam at CERN in April of 1998. The standard RD42 silicon reference telescope [14] was used to provide a reference trajectory for charged particles passing through the detector. The diamond was operated at 550 V corresponding to an electric field of 0.9 V/$\mu$m. We collected 200,000 tracks at normal incidence to the diamond surface and have studied the pixel hit distribution, charge deposition and spatial correlations between the pixel detector and the tracks in the external reference telescope.

### 6.1 Charge Particle Hit Distribution

Figure 5 shows the number of hits found per pixel during this test. The area of the boxes is proportional to the number of tracks above threshold in each pixel cell. The most

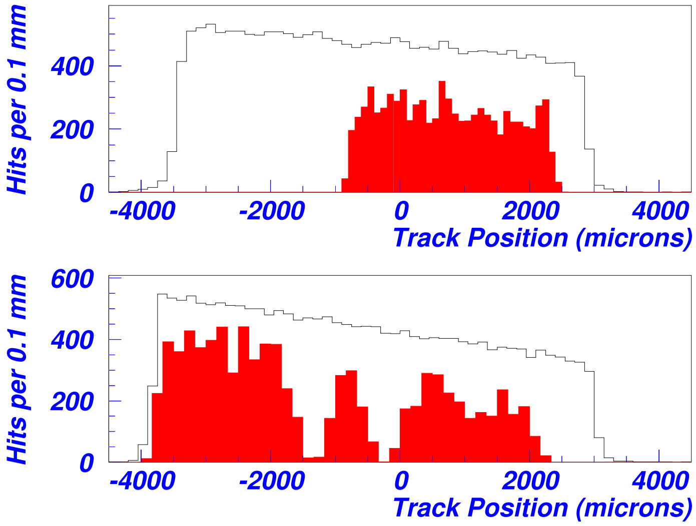


Figure 6: Spatial distribution of tracks projected on the diamond pixel detector (open histogram). Distribution of hits reported by the diamond pixel detector (shaded histogram), for rows in the pixel detector (top) and columns (bottom). The relative normalisation of these two distributions is arbitrary. In the upper plot one can clearly see the 3.2 mm wide pixel detector while in the lower plot the removal of the noisy columns (4 and 6) can be seen clearly as dips in the number of hits.

striking feature of Fig. 5 is that hits have been recorded in almost all of the pixel cells. This is better evidence that a high bump-bonding yield had been achieved (we discuss the correlation of these hits with tracks from the reference telescope below). A study of the hit distribution in columns 4 and 6 indicated that many of these hits were due to noise rather than real charged particle signals, due to the low threshold in these two columns. We excluded these columns from further study. There are also a larger number of hits in the even columns than in adjacent odd columns of the detector. This was due to threshold differences between even and odd columns. In addition there is a reduction in the number of hits seen on the “right” side (columns 7-10) of the detector when compared to the “left” side (columns 0-3). This resulted from a reduction of the beam intensity towards that side of the detector. In Fig. 6, we show a comparison of the spatial distribution of all tracks seen in the telescope to the hits found in the diamond pixel detector. In this figure, the diamond hit positions are plotted in the telescope coordinate system. In both views the diamond hit distribution follows the incident beam distribution.

Figure 7 shows a projection of the number of hits seen in each pixel. In the top plot, we see that there are 26 pixels that failed to record a single hit. In the lower plot, we restrict our attention to columns 0-3 of the detector. There only 6 of the 256 pixels failed to record a hit. From the lower plot it is clear that there is very little chance that any of these six were a fluctuation. A background subtraction, based on a smooth extrapolation

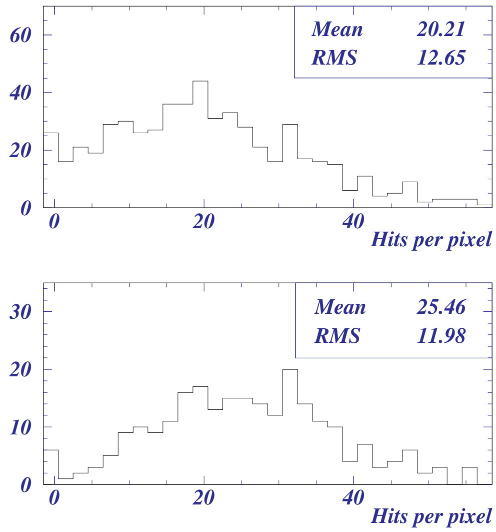


Figure 7: Distribution of number of hits per pixel cell seen in the testbeam. The top plot shows the distribution over the whole detector (512 cells in columns 0-3 and 7-10) while the bottom plot shows the number of hits per cell only on the "left" side of the detector where a significantly higher number of hits per cell have been recorded.

through the single pixel that recorded only one hit indicates that less than one of the six missed pixels was the result of a fluctuation. Further, all of the missed pixels are at the edge of the detector consistent with the difficulty of metallising small samples near their edges. Two of the non-responding pixels were observed to be missing before the bonding process and a third is a special channel in the readout chip that is not active to allow direct access to the analog signal from the front-end preamplifier. From this data and these *a-priori* observations of channels not expected to be functioning, we conclude that at least 99% (250/253) of the channels were successfully bonded and capable of recording hits. A similar conclusion can be drawn from the top distribution. In that case, a background subtraction, based on the number of cells with only a few hits recorded, of about 15 channels is necessary. This leaves 11 channels (26-15) that appear to lack hits leading us to conclude that 98% (501/509) of the channels were successfully bump-bonded.

## 6.2 Charge Distribution

The diamond material that we used for this pixel detector had been previously tested as a strip tracker (see Section 3). As such, we had previously measured the charge distribution and can predict the expected behaviour of the pixel detector. Figure 8a) shows the charge observed in the pixel detector measured using the TOT feature of the ATLAS/3 readout chip. Figure 8b) summarises our understanding of the situation. The gray histogram is the charge collected on single strips when this diamond was tested as a strip tracker with 50 $\mu$m pitch. The single-strip charge is all that is relevant to the pixel detector as we expect, and observe, all hits to be in single pixels. The single-strip data was taken with the

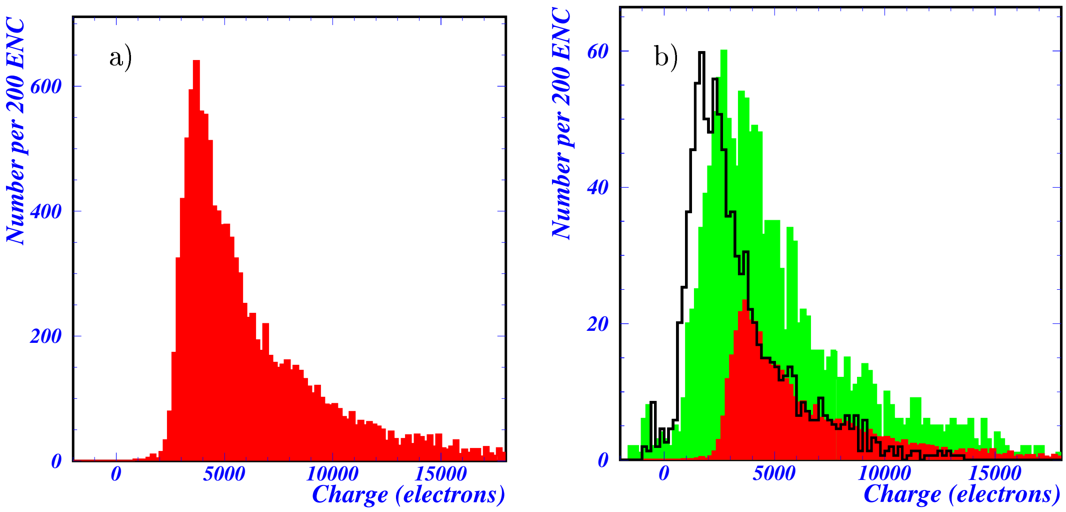


Figure 8: a) Distribution of TOT (charge) measurements for triggered pixels in the 1998 testbeam. b) Comparison of the charge observed in the pixel detector (black histogram) with that seen in the same diamond when it was instrumented as a strip tracker in 1997 (gray histogram). The open histogram is a prediction, based on the observed (gray) single-strip charge and the fact that the diamond was not pumped in the test of the pixel detector.

tracker fully pumped. As stated earlier, we were reluctant to operate the diamond pixel detector fully pumped and at full voltage as a precaution against damaging the readout electronics. Extensive study of the pumping effect leads us to conclude that sensors in the un-pumped state produce 40% less charge. A prediction for this distribution is shown as the open histogram of Fig. 8b). Overlaid (in black) is the actual charge observed in the pixel detector, suitably normalised. The agreement is quite good.

### 6.3 Detector Efficiency

By taking the ratio of the predicted distribution (in the open histogram) and the observed charge distribution (from the black histogram) in Fig. 8b), we extract a measure of the pixel sparsification threshold. Figure 9 shows this ratio. We see a threshold onset just above 2,500 $e$ that continues to rise until almost 4,000 $e$. We conclude that this detector operated with an average threshold of 3,200 $e$, the 50% point on this curve.

Of the 155,000 fully reconstructed testbeam tracks, the trigger acceptance calculation predicts 55,000 of them passed through the diamond pixel detector. Since we excluded two noisy columns, we should have observed 44,000 tracks. Given a threshold of 3,200 $e$ and the unpumped diamond charge distribution, we expect $\approx$ 16,000 hits. We observe 14,800 hits consistent with the number expected. The operating threshold in the testbeam was slightly lower than in the source test described earlier, but still higher than optimal.

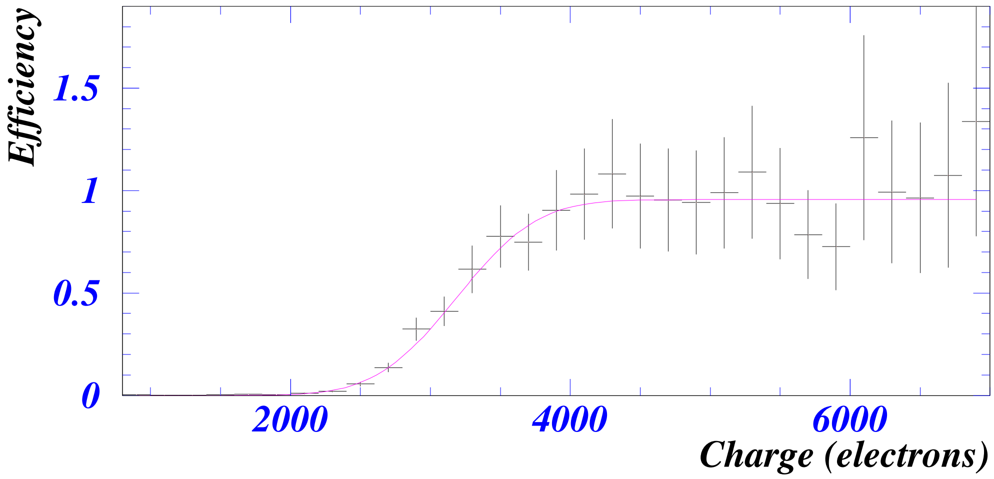


Figure 9: Ratio of the charge observed in the diamond pixel detector (Fig. 8a) to that predicted from prior strip tracker tests with this same diamond (open histogram in Fig. 8b). The curve rises to 50% at 3,200 $e$ and has a dispersion of 450 $e$, reaching full efficiency at 4,000 $e$.

### 6.4 Spatial Resolution

In order to measure the spatial resolution of the pixel detector, the testbeam setup was equipped with a reference telescope [14]. The telescope has eight planes of 50 $\mu$m pitch silicon strip detectors with floating intermediate strips arranged in two sets of four planes 180 mm apart. The silicon strip detectors are read out by VA2 strip electronics [7]. The pixel detector was placed between the silicon reference planes. The difference between the measured position of a hit in the pixel detector and a beam particle track fit using only the reference planes gives a position residual. The standard deviation of the position residual distribution is a measure of the spatial resolution for the pixel detector. The standard deviation of the silicon detector residuals was found to be 2 $\mu$m. The pixel detector was aligned to the coordinate system of the telescope. This alignment corrects for a shift in the direction perpendicular to the long pixel and a rotation around the beam axis.

A comparison of the reference telescope track positions and the position of hits recorded in the pixel detector is shown in Figs. 10a) and 10b). A clear correlation between the two measurements is seen. After the silicon reference telescope and pixel detector coordinate systems have been aligned, we observe the residual distributions shown in Figs. 11a) and 11b). The spatial resolution along the direction of the large pixel dimension (536 $\mu$m in length) is, as expected, a top-hat distribution with a full width at half maximum of slightly over 500 $\mu$m. In the direction measured by the small pixel dimension, we see a position resolution, 14.8 $\mu$m, consistent with the strip pitch divided by the square root of twelve, the digital hit resolution expected from single pixel hits. In both cases, there are minimal tails indicating that very few of the hits recorded by the pixel detector were unrelated to the charged tracks measured in the telescope. The flux of beam particles through our telescope is such that fewer than 1% of the triggers contain more than one charged track, thus the potential for confusion in the reconstruction of the reference telescope, while

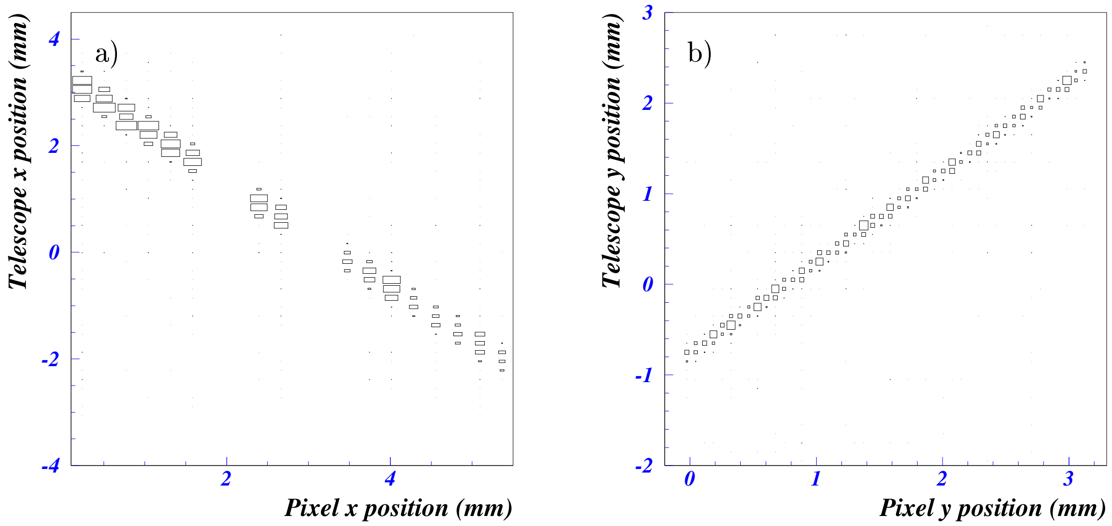


Figure 10: The spatial correlation between the pixel detector hits and the reference telescope tracks in a) the $x$ (long pixel) view (note that the noisy columns have been removed) and b) the $y$ (short pixel) view.

minimal, is not completely negligible. However, it should be clear that the majority (over 99%) of the hits that trigger the pixel readout chip result from the passage of charged particles also reconstructed by the silicon reference telescope. This is the best evidence that most of our pixel cells were successfully bump-bonded and functioning during these tests.

## 7 Summary and Conclusions

We have built a working diamond pixel detector bump-bonded to prototype LHC electronics. As diamond is sufficiently radiation hard to survive at small radii for the lifetime of LHC experiments, it is natural that it be considered for geometries close to the interaction region.

Work with the ATLAS/3 pixel readout chip has yielded a fully functional prototype that has proven high bump-bonding yields are possible. We conclude that more than 98% of the pixels in our prototype device were successfully bump-bonded. We have observed hits in the diamond pixel detector that are correlated to charged tracks measured in our reference telescope. We have shown a position resolution of better than 15 $\mu$m, consistent with the digital resolution expected for this device.

These results have encouraged us to develop new detectors with higher quality CVD material. The new devices, with 50% more signal are being bonded to improved readout chips with lower thresholds. With such improvements in detector material quality and the reduction of readout thresholds – similar to those that will be needed to readout thinned silicon sensors – our goal of producing a CVD diamond based pixel detector system appears

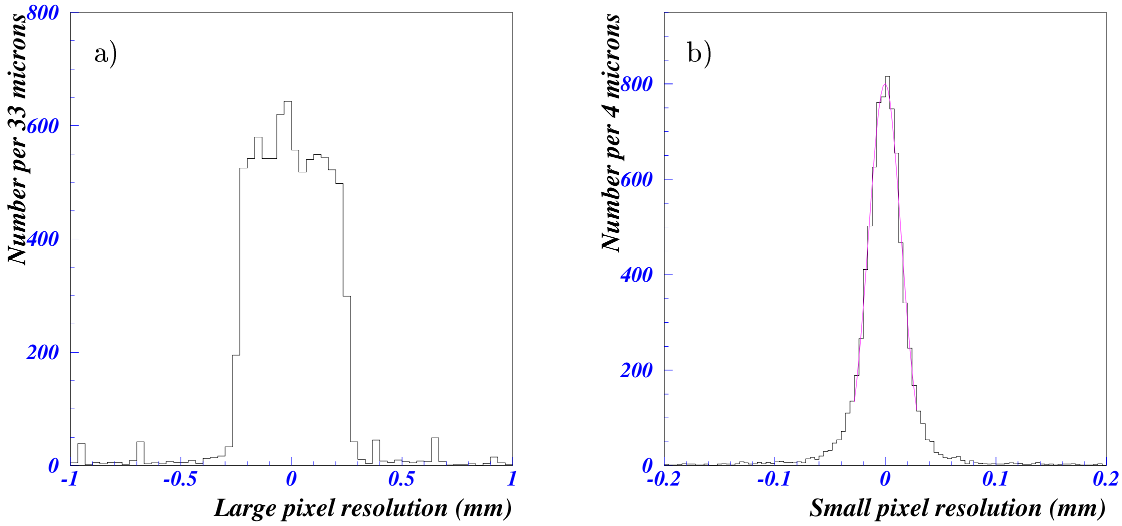


Figure 11: The position resolution of the diamond pixel detector prototype in a) the $x$ (long pixel) view and b) the $y$ (short pixel) view. The curve through the data in b) is a fit to a Gaussian distribution with a sigma of 14.8 $\mu$m.

to be achievable in the near future.

## References

[1] ATLAS Collaboration, "Inner Detector TDR", CERN/LHCC/97-17, (1997).

[2] CMS Collaboration, "CMS Tracker TDR", CERN/LHCC/98-6, (1998).

[3] BTeV Collaboration, "Expression of Interest for a Heavy Quark Programme", FNAL-660, (1997).

[4] RD42 Collaboration, CERN/LHCC/97-3, P56, (1996).

[5] ATLAS Collaboration, "Pixel Detector TDR", CERN/LHCC/98-13, (1998).

[6] F. Borchelt *et al.*, Nucl. Instrum. and Meth. **A354**, (1991), 506.

[7] Integrated Detector and Electronics AS, Hovik, Norway.

[8] Boeing Defense and Space Group, Anaheim, California, U.S.A.

[9] DeBeers Industrial Diamond Division, Charters, Ascot, England.

[10] S. Zhao, Ph.D. Thesis, The Ohio State University, (1994).

[11] M.A. Plano *et al.*, Appl. Phys. Lett. **64**, (1994) 193.

[12] D. Meier, Ph.D. Thesis, University of Heidelberg, (1999).

[13] Ref. [1], p309; and Ref. [5], pp126 and 236.

[14] C. Colledani *et al.*, Nucl. Instrum. and Meth. **A372**, (1997), 3.